Science of the Total Environment 778 (2021) 146248

Contents lists available at ScienceDirect

Science of the Total Environment

journal homepage: www.elsevier.com/locate/scitotenv

Review

A review of measurement techniques for aerosol effective density

Long Peng [a,d,e], Zongrui Li [b], Guohua Zhang [a,c,*], Xinhui Bi [a,c], Weiwei Hu [a,c], Mingjin Tang [a,c], Xinming Wang [a,c], Ping'an Peng [a,c], Guoying Sheng [a]

[a] State Key Laboratory of Organic Geochemistry and Guangdong Provincial Key Laboratory of Environmental Protection and Resources Utilization, Guangzhou Institute of Geochemistry, Chinese Academy of Sciences, Guangzhou 510640, China
[b] State Environmental Protection Key Laboratory of Environmental Pollution Health Risk Assessment, South China Institute of Environmental Sciences, Ministry of Ecology and Environment, Guangzhou 510655, China
[c] Guangdong-Hong Kong-Macao Joint Laboratory for Environmental Pollution and Control, Guangzhou Institute of Geochemistry, Chinese Academy of Sciences, Guangzhou 510640, China
[d] Institute for Environmental and Climate Research, Jinan University, Guangzhou 511443, China
[e] University of Chinese Academy of Sciences, Beijing 100049, China

HIGHLIGHTS

- Measurement techniques for aerosol effective density are comprehensively reviewed.
- Typical principles, errors and field applications of each technique are presented.
- Advantages and disadvantages of each technique are discussed.
- Further improvements for aerosol density measurements are proposed.

GRAPHICAL ABSTRACT

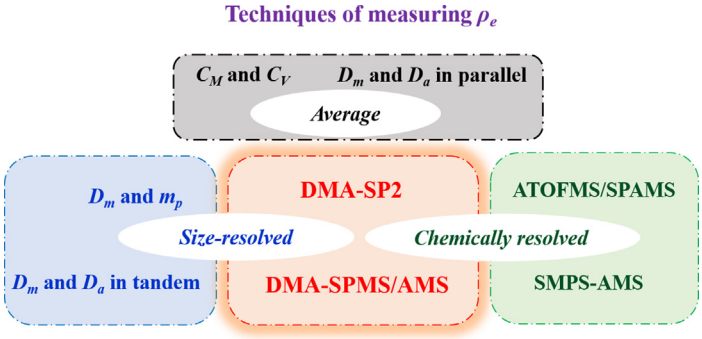

ARTICLE INFO

Article history:
Received 10 December 2020
Received in revised form 25 February 2021
Accepted 27 February 2021
Available online 10 March 2021

Editor: Jianmin Chen

Keywords:
Particle
Effective density
Size
Chemical compositions
Application

ABSTRACT

Density (ρ) is one of the most important physical properties of aerosol particles. Owing to the complex nature of aerosols and the challenges of measuring them, effective density (ρ_e) is generally used as an alternative measure. Various methods have been developed to quantify the ρ_e of aerosols, which provide powerful technical support and understanding of their physical properties. Here, we present a comprehensive review of the characterisation techniques of ρ_e currently used in the literature. Overall, six categories of measurement are identified, and the typical configuration, measurement principles, errors and field applications of each are demonstrated. Their respective advantages and disadvantages are also discussed to improve their application. Finally, we outline future directions for further technical improvement in, and instrumental development for, ρ_e measurement.

* Corresponding author at: State Key Laboratory of Organic Geochemistry and Guangdong Provincial Key Laboratory of Environmental Protection and Resources Utilization, Guangzhou Institute of Geochemistry, Chinese Academy of Sciences, Guangzhou 510640, China.
E-mail address: zhanggh@gig.ac.cn (G. Zhang).

https://doi.org/10.1016/j.scitotenv.2021.146248
0048-9697/

Contents

1. Introduction

Atmospheric aerosols are liquid or solid particles with sizes ranging from a few nanometers to microns. They can be emitted into the atmosphere from both natural and anthropogenic processes, such as sea spray, volcanic eruptions, biomass burning, and fossil fuel combustion (Finlayson-Pitts and Pitts Jr, 1999; Seinfeld and Pandis, 2016). In addition, aerosols can be formed by gas-solid transformation in the atmosphere (i.e., new particles formed by nucleation and condensation of gaseous precursors) and heterogeneous reaction processes (Poschl, 2005; Seinfeld and Pandis, 2016). Depending on their physical and chemical properties, aerosols behave differently and play a profound role in air quality, human health, and global climate (Buseck and Posfai, 1999; Poschl, 2005). However, the quantification of these impacts remains challenging because of their complex and ever-changing nature.

Density (ρ) is one of the most important physical properties of particles because it influences transport properties and, therefore, the fate of particles in both the atmosphere and the human respiratory system (Liu and Daum, 2008; Seinfeld and Pandis, 2016). Two definitions of density are applied to characterise the properties of particles, including particle density (ρ_p) and material density (ρ_m). ρ_p is calculated through dividing particle mass (m_p) by particle volume (V_p) which is determined by all material and void space enclosed within the particle envelope, while ρ_m is calculated through dividing by m_p by material volume (V_m) which is only determined by all material in the particle. ρ_p is linked to optical properties (Tang and Munkelwitz, 1994), and Liu and Daum (2008) found the ρ_m played a dominant role in the effects on refractive index. Koch et al. (2009) reported that variations in the ρ_p of black carbon (BC) between 1.0 and 2.0 g cm^{-3} might lead to large fluctuations in aerosol radiative forcing. Moreover, ρ_p is an indispensable parameter for determining the relationship between the mobility diameter (D_m) and aerodynamic diameter (D_a), and for converting high time-resolved ambient particle number distributions to mass concentrations related to air quality and visibility (Hu et al., 2012; McMurry et al., 2002; Morawska et al., 1999).

While aerosol ρ_m can be deduced from composition-resolved densities, direct measurements are much more reliable for, in particular, the complex nature of atmospheric aerosols. At present, the ρ_p of spherical particles can be derived through the combination of optical diameter (D_o) and D_a (Cross et al., 2007; Murphy et al., 2004), and the combination of D_m and vacuum aerodynamic diameter (D_{va}) (Katrib et al., 2005; Zelenyuk et al., 2008c). For aspherical particles, Park et al. (2004a, 2004b) presented methods for measuring ρ_p based on particle mass (m_p) and volume (V), and Vaden et al. (2011) used D_{va} and the detection efficiency of aerodynamic lenses to obtain ρ. However, the acquisition of V can only be used for diesel soot aggregates based on empirical calculations, and the detection efficiency of this can only be applied to a small range of particles with a D_{va} of approximately 100 nm, which limits wider application in the ambient atmosphere.

Limited by the techniques of the measurement of the ρ for aspherical aerosol particles, effective density (ρ_e) has been commonly adopted as an alternative to ρ_p (Katrib et al., 2005; Sumlin et al., 2018), which accounts for a dynamic shape factor (χ) for parameterising the morphology of the particles (Yon et al., 2015). ρ_e intimately connects to the dynamic, morphological, and chemical properties of the particles, and serves as a link between the important characteristics of aerosol particles between, for instance, its volume equivalent diameter (D_{ve}) and D_a, or between its ρ_p and χ (Nosko and Olofsson, 2017). It is also used to track the atmospheric processing of particles, such as new particle formation (Guo et al., 2014; Yin et al., 2015) and compositional transformations during chemical reactions (Katrib et al., 2005; Liu et al., 2015). Recently, ρ_e was also found to be highly correlated with the particle refractive index that directly determines aerosol optical properties (Zhao et al., 2019).

There are three definitions of ρ_e, for which the theoretical basis has been systematically reviewed by DeCarlo et al. (2004). Briefly, the first definition (ρ_e^I) is the ratio of the measured particle mass (m_p) to the apparent volume (V_a), calculated assuming a spherical particle with D_{ve} equal to the measured D_m, as shown in Eq. (1):

$$\rho_e^I = \frac{6m_p}{\pi {D_m}^3}. \tag{1}$$

The second definition (ρ_e^{II}) is the ratio of D_m and D_{va}, expressed as:

$$\rho_e^{II} = \frac{D_{va}}{D_m}\,\rho_0, \tag{2}$$

where ρ_0 represents a unit density of 1.0 g cm^{-3}.

The third definition (ρ_e^{III}) is the ratio of ρ_p to χ, which is expressed as:

$$\rho_e^{III} = \frac{\rho_p}{\chi}. \tag{3}$$

Various techniques have been developed to obtain the ρ_e of aerosols, such as the aerodynamic aerosol classifier (AAC)-scanning mobility particle spectrometer (SMPS) (Tavakoli and Olfert, 2014) and measuring both the D_m and D_a size distributions (Khlystov et al., 2004). As a frequently used technique, the differential mobility analyser (DMA)-centrifugal particle mass analyser (CPMA)-condensation particle counter (CPC) has been applied to characterise the aerosols emitted from various primary emissions, such as light-duty vehicles (Quiros et al.,

2015a) and biomass combustion activities (Bullock and Olfert, 2014; Dastanpour et al., 2017; Kazemimanesh et al., 2019). The approach has also been used to determine the ρ_e of particles in the atmosphere of Riverside, CA (Lin et al., 2018) and Beijing, China (Qiao et al., 2018), which is important for understanding the complex properties of aerosols and, thus, their fate and roles in the atmosphere.

Previously, DeCarlo et al. (2004) introduced mathematical formulas for the definition of ρ_e and broadly illustrated the measurement techniques used in previous studies pre-2004; Schmid et al. (2007) briefly discussed some of the most frequently used instruments for measuring ρ_e^I and ρ_e^{II}; and Pratt and Prather (2012) focused on measurement techniques for ρ_e^{II} by combining SMPS with aerosol mass spectrometry. To our knowledge, there have been no reviews that comprehensively summarise more recent advances in the measurement of ρ_e.

To address this gap, here we summarise the techniques available for measuring the ρ_e of aerosols. In each case, we focus on experimental setup configurations, illustrate the measurement principles, and briefly summarise the advantages and disadvantages. According to the technical principles of measurement, all techniques are classified into six categories, as presented in Sections 2 to 4. Section 2 covers four categories of methods for measuring ρ_e^I, while Sections 3 and 4 describe methods for measuring ρ_e^{II} and ρ_e^{III}, respectively.

2. Obtaining ρ_e^I from concurrent measurements of mass and volume

Theoretically, ρ_e^I can be obtained by simultaneously measuring the m_p and V_a of the target particles, as defined in Eq. (1). This is the most commonly used approach. Table 1 lists the current techniques that are applicable to the measurement of m_p and V_a. For m_p, there are four main measurement methods to retrieve ρ_e^I, including: (i) measurement of the mass concentration (C_M), (ii) measurement of the m_p of individual particles, (iii) indirectly obtaining m_p by measuring the D_a and D_m of particles, and (iv) measuring the m_p of soot. Each of these approaches is discussed in the following sections with respect to retrieving ρ_e^I.

2.1. Mass and volume concentration

The mean ρ_e^I of the target particles can be directly calculated by their C_M and volume concentration (C_V), which was first proposed by Pitz et al. (2003). Particle C_M can be directly measured by a tapered element oscillating microbalance (TEOM) or obtained by weighing the filters collected by micro-orifice uniform deposit impactor (MOUDI), and C_V can be derived from the number-based size distribution with instruments such as a SMPS.

Four methods for combining TEOM and other techniques for C_V derivation have been applied to characterise particle ρ_e^I. The first approach measures the D_m number distribution from 10 to 500 nm using a differential mobility particle spectrometer (DMPS) and the D_a number distribution between 0.1 and 3 μm using a laser aerosol spectrometer (LAS-X), as described by Pitz et al. (2003). C_V is estimated by integrating the volume size distribution from 0.01 to 2.03 μm in D_m (where the upper integration threshold of 2.03 μm corresponds to the D_a of 2.5 μm, assuming a ρ_e^I of 1.5 g cm^{-3}). The second method improves the accuracy of the calculation by altering the lower integration threshold of D_m to 3 nm using a twin differential mobility particle sizer (TDMPS) (Pitz et al., 2008). Combined with the measurement of C_M, high temporal resolution ρ_e^I data for aerosol particles were successfully obtained for Augsburg, Germany using this approach; Fig. 1 shows that diurnal variation of ρ_e^I for both weekdays/weekends and winter/summer were similar, with a minimum ρ_e^I occurring the morning and afternoon (approximately 1.5 g cm^{-3}) and a maximum ρ_e^I (near 1.8 g cm^{-3}) occurring at midday (Pitz et al., 2008). The minimum ρ_e^I was related to traffic soot particles from fresh primary aerosol emissions, especially in the early morning hours of weekdays, while maximum ρ_e^I values were attributed to increased secondary and aged particles (Pitz et al., 2008). These observations imply that ρ_e^I has potential as an indicator of chemical composition and atmospheric processing. The third method, developed by Nosko and Olofsson (2017), obtains C_V using a fast mobility particle sizer (FMPS) for the particles with diameters of 0.0056–0.56 μm and an optical particle sizer (OPS) for particles with diameters of 0.3–10 μm. Based on this method, these authors determined that the ρ_e^I of the wear particles generated from car brake materials was 0.75 ± 0.2 g cm^{-3}. The fourth method uses the SMPS-aerodynamic particle sizer (APS) system to determine C_V (Cha and Olofsson, 2018b). In this case, ambient observations showed that the ρ_e^I of particles in a railway tunnel environment had a diurnal average value of approximately 1.87 g cm^{-3}. Using the same method to obtain C_V, Liu et al. (2015) measured C_M using a TEOM with a filter dynamic measurement system (FDMS) for both non-volatile and semi-volatile particulate matter in Beijing. They found that ρ_e^I had daily average values of 1.41 ± 0.40 and 1.60 ± 0.43 g cm^{-3} in the cold and warm seasons, respectively.

The C_M of size-segregated aerosols can be further obtained by a MOUDI. To characterise size-resolved particle ρ_e^I in the atmosphere of Beijing, Hu et al. (2012) used a MOUDI to measure particulate C_M. They obtained C_V using a combination of the D_m number size distributions in the 3–700 nm range and a TDMPS and by measuring the D_a number distribution in the size 0.6–10 μm range with an APS. Their results indicated that ρ_e^I increased with diameter from approximately 1.5 g cm^{-3} at 0.1 μm to >2.0 g cm^{-3} in the coarse mode. This approach could also be applied to estimate the χ of particles when the chemical information of the collected aerosols is included. As shown in Fig. 2, particle χ in Beijing was found to vary between 0.95 and 1.13 based on values of ρ_e^I and ρ_m. Similarly, Lin et al. (2015) determined the ρ_e^I of ultrafine particles (UFPs, with diameters <100 nm) through a SMPS-MOUDI setup in which a MOUDI measured the C_M and a SMPS measured the D_m number distribution. Lin et al. (2015) found that the ρ_e^I and χ values of UFPs in Northern Taiwan were 0.68 ± 0.16 g cm^{-3}and 2.06 ± 0.19, respectively. The main difference between a MOUDI and a TEOM is that TEOMs do not require a filter, giving the advantage of higher temporal resolution in the measurement of C_M. In contrast, MOUDI method can provide addition chemical information through analysis of the collected

Table 1
Techniques for measuring the m_p and V_m of particles.

	Techniques for measuring m_p (range)	Techniques for measuring V_m (range)	
C_M	TEOM (FDMS) ($PM_{2.5}$) MOUDI (decided by cutsizes) QCM (fractions of nanograms - micrograms)	D_m size distribution DMPS (10–500 nm) TDMPS (3–700 nm) FMPS (5.6–560 nm) SMPS (14–710 nm)	D_a size distribution LAS-X (0.1–3 μm) APS (0.6–10 μm) OPS (0.3–10 μm)
m_p	Nano-PMC (20 × 10^{-21} g-0.5 × 10^{-18} g) CPMA/ APM (0.2× 10^{-18}-1.05× 10^{-12} g) MAAP (0–60 μg m^{-3} BCE)	DMA	
D_a and D_m	(1) AAC-SMPS (2) DMA-ELPI (3) DMA-SELPI (4) SMPS/FMPS-APS/ELPI/CEPI		
m_p of soot	SP2 (10 ng m^{-3} BCE)	(VT)DMA	

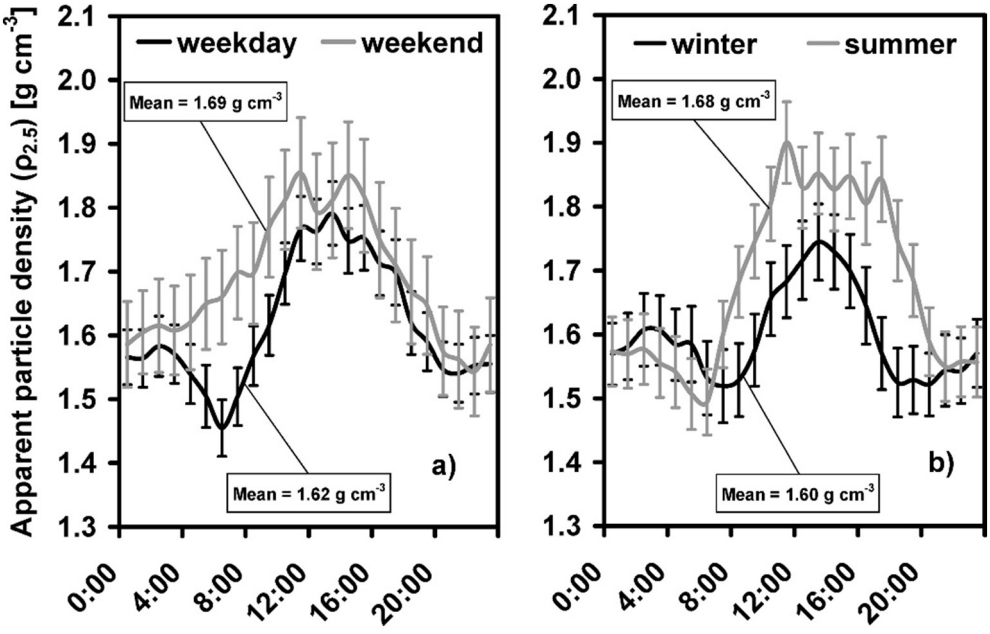

Fig. 1. (a) Diurnal variations in ρ_e^I for weekdays and weekends. (b) Diurnal variations of ρ_e^I in the summer and winter seasons. Reprint with permission by Pitz et al. (2008). Copyright 2008 American Chemical Society.

particles, and therefore, MOUDI-based methods have the advantage of obtaining both ρ_m and χ.

Table 1 summarises the techniques available for measuring the D_m- and D_a-based size distributions and applicable size ranges. The combination of any two techniques can achieve derive C_V, providing multiple possibilities for obtaining ρ_e^I using these methods. In addition, these methods can provide a reference ρ_e^I value for conversion between C_M and C_V. A major drawback of this approach is that the obtained ρ_e^I represents the average value for particles of multiple sizes and chemical compositions, which limits application. The relationship with particle size can be considered using a DMA-aerosol particle mass analyser (APM)-CPC. Based on this technique, Yin et al. (2015) found that the average ρ_e^I of atmospheric particles increased from 1.36 g cm^{-3} at D_m 50 nm to 1.55 g cm^{-3} at D_m 400 nm. However, the use of mass and volume concentrations is based on the assumption that ρ_e is 1.5 g cm^{-3} for the conversion between D_m and D_a. Such an assumption might lead to errors because ρ_e widely varies and has not yet been accurately evaluated.

In addition, Sarangi et al. (2016) developed a setup of a SMPS-quartz crystal microbalance (QCM) to determine ρ_e^I using the a SMPS and a QCM to obtain the particle size distribution of D_m and the corresponding

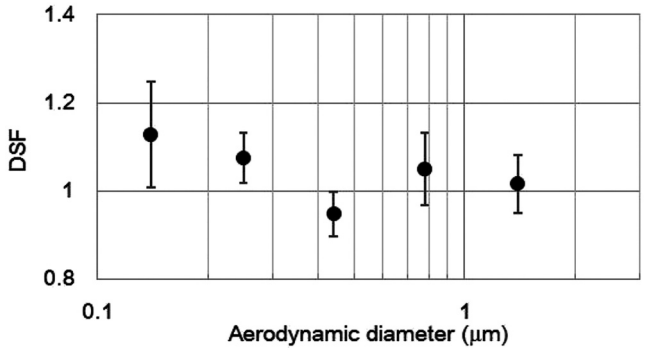

Fig. 2. Dynamic shape factors of particles with D_a ranging from 0.1 to 1.8 μm. Reprint with permission by Hu et al. (2012). Copyright 2012 American Chemical Society.

C_M, respectively. These authors successfully obtained the ρ_e^I for ambient particles at the beginning of the winter period in New Delhi (1.28 ± 0.12 g cm^{-3}). The error of this approach was determined to be in the range of 9–17% based on the ρ_e^I of aspherical particles, while theoretical values were inconclusive. Therefore, the reliability of this technique should be further evaluated by measuring the ρ_e^I of spherical particles that can be fully validated.

2.2. Particle mass scanning for specific sizes

The nanoparticle mass classifier (nano-PMC) and CPMA/APM are capable of classifying particles with a specific mass-to-charge ratio. For particles with a single charge, nano-PMC is applied to classify particles with m_p ranging from 20×10^{-21} g to 0.5×10^{-18} g (Brossell et al., 2015), while CPMA/APM deals with particles with an m_p range of 0.2×10^{-18} to 1.05×10^{-12} g. Fig. S1 shows a schematic diagram of the DMA-mass classifier-CPC setup. To calculate ρ_e^I, particles with a specific D_m are first classified using a DMA followed by measuring the m_p with the mass classifiers. The classified particles are associated with both single and multiple charges. Then, the mass classifier screens the classified particles with a specific mass-to-charge ratio and transmits them into the CPC, which records the number concentration of the monodisperse particles. The particles with multiple charges are excluded during the transmission within the instrument. This is because the mass-to-charge ratio set by the mass classifier is based on a linear relationship between the charges and m_p (Eq. (4)), yet the m_p of the particles (~D3 m) from the DMA is not linearly correlated with the charges (Eq. (5)).

$$\frac{m_p}{N} = \frac{eV_0}{\left(\frac{R_2+R_1}{2}\right)^2 \varpi^2 In(R_2/R_1)}, \tag{4}$$

$$\frac{D_m}{NC_c(D_m)} = \frac{2V_0Le}{3\mu(Q_a + Q_{sh})In(R_4/R_3)}, \tag{5}$$

where e, V_o, μ, N, Q_a, and Q_{sh} represent elementary charge, voltage, gas viscosity, the number of charges, aerosol flow, and sheath flow, respectively; ω, R_1, and R_2 represent the rotational speed, inner cylinder radius,

and outer cylinder radius of the operating space in the CPMA, respectively; L, R_3, and R_4 represent rod length, inner radius, and outer radius of the DMA annular space, respectively. Therefore, only particles with a single charge can escape from the mass classifier, which means the m_p of the particles is obtained. By stepping the voltage and/or rotational speed of the mass classifier, the particle number concentration is recorded as a function of the m_p of the particles using a CPC. The peak m_p of the particles is then obtained using Gaussian fitting.

The CPMA/APM setup follows the same principle when measuring particles possessing a certain mass-to-charge ratio, which is achieved by balancing the centrifugal and electric field forces on the particle. The major difference is that the CPMA consists of two concentric cylinders rotating at different angular velocities while the velocities for the APM are the same. The improvement in the concentric cylinder makes the forces in the equilibrium radius more stable within the operating space in the CPMA, which improves the transfer function of the instrument (Olfert and Collings, 2005; Olfert et al., 2007).

Approximately 50 studies (Tables S1 and S2) have used this method to characterise the ρ_e^I of particles from primary emissions sources and in the atmosphere since 2004. This includes particles emitted from motor vehicles and engines (Fujitani et al., 2016; Momenimovahed and Olfert, 2015; Quiros et al., 2015a; Quiros et al., 2015b; Zelenyuk et al., 2014) and biomass combustion (Dastanpour et al., 2017; Fujitani et al., 2016; Kazemimanesh et al., 2019; Li et al., 2016; Malik et al., 2011; Zhai et al., 2017), yielding ρ_e^I values generally less than 1.0 g cm^{-3} This might be caused by the voids in these particles as well as their irregular shape (Hu et al., 2012; Leskinen et al., 2014; Pei et al., 2018). The ρ_e^I of particles in urban atmospheres ranges from 0.10 g cm^{-3} to 1.70 g cm^{-3} based on studies in Beijing (Qiao et al., 2018), Shanghai (Xie et al., 2017; Yin et al., 2015), Nanjing (Ma et al., 2017), Nagoya (Nakagawa et al., 2016; Nakayama et al., 2014), Copenhagen (Rissler et al., 2014), on the California-Mexico border (Levy et al., 2014), Riverside, CA (Lin et al., 2018), and various locations in the Los Angeles Basin (Geller et al., 2006). Such variability is influenced by particle morphology, the primary emission sources involved, and the degree of aging (Schnitzler et al. (2014). For example, Fig. 3 shows the size-resolved ρ_e^I of initial and coated soot aggregates, with higher values for the coated soot aggregates attributed to the formation of secondary organic aerosols on the initial soot aggregates (Schnitzler et al., 2014).

To reduce the sampling time and improve sampling frequency, the setup of DMA-CPMA/APM-CPC can be reversed into APM/CPMA-DMA-CPC. This first selects the particles with a specific mass-to-charge ratio

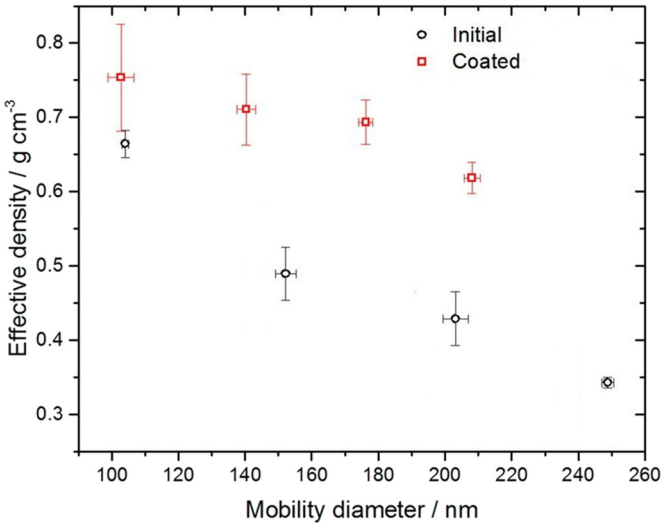

Fig. 3. ρ_e^I of soot aggregates before (initial) and after (coated) restructuring due to SOA derived from p-xylene.
Reprint with permission by Schnitzler et al. (2014). Copyright 2014 American Chemical Society.

using CPMA/APM and then obtains the peak D_m from the downstream SMPS to determine ρ_e^I (Leskinen et al., 2014; Malloy et al., 2009). According to the different setting parameters, each measurement cycle of a DMA-CPMA/APM-CPC setup takes approximately 30–60 min (Malloy et al., 2009; Qiao et al., 2018). This reversed setup can shorten the sampling time because the DMA-CPC (i.e., SMPS) completes the D_m size distribution measurement more quickly. Similarly, ρ_e^I could also be obtained using a differential mobility spectrometer (CPMA-DMS) (Johnson et al., 2015a; Johnson et al., 2015b) as the D_m size distribution can also be obtained by DMS. However, the reversed technique is not widely used because most studies have focused on the variation of ρ_e^I with particle size rather than particle mass.

A notable advantage of the DMA-CPMA/APM-CPC setup is the accurate determination of aerosol ρ_e^I owing to the accuracy of DMA and CPMA/APM in characterising the D_m and m_p, respectively. Using this setup to measure Polystyrene Latex (PSL) particles with different sizes (with a ρ_p of 1.05 g cm^{-3}) obtained an average density is 1.04 ± 0.01 g cm^{-3} within an error of 2% (Qiao et al., 2018). The other major advantage of this approach is the ability to establish a relationship between particle size and ρ_e^I, as size-resolved ρ_e^I is measured. For example, the ρ_e^I of primary soot particles was found to decrease with particle size from 1.28 g cm^{-3} at 20 nm to 0.22 g cm^{-3} at 500 nm (Olfert and Rogak, 2019). In contrast, Sumlin et al. (2018) found that the magnitude of ρ_e^I for nascent brown carbon was broadly independent of particle size. However, particles with different chemical components, in particular organics, have a wide range of ρ_e. For example, the ρ_e of secondary organic aerosols formed during the ozonolysis of cycloalkenes and biogenic hydrocarbons and the photooxidation of m-xylene range from 0.64 to 1.45 g cm^{-3} (Bahreini et al., 2005). Therefore, the lack of ability to distinguish chemical constituents still limits the application in the characterisation of complicated aerosol populations. Specifically, this setup can obtain single-charge particles for the pure materials yet the measurement of ρ_e may be affected by the multiple charges of aerosols in the atmosphere as particles with diverse chemical compositions may have a wide range of ρ_e properties (Rissler et al., 2013).

In addition, Jeong and Lee (2017) developed a method to measure the ρ_e^I of the BC-core using a SMPS-multi-angle absorption photometer (MAAP). In this approach, classified particles with a specific D_m from the DMA are split into a MAAP and a CPC. The MAAP and CPC measure the mass concentration of the BC-core particles (C_{BC}) and the number concentration (N) of the monodisperse particles, respectively. The C_{BC} and N are then used to calculate the mass of the BC-core (m_{BC}), which is combined with D_m to obtain ρ_e^I. However, this technique has limited applicability in the characterisation of atmospheric particles because the MAAP can only measure C_{BC} and the CPC cannot selectively measure the number concentration of BC particles.

2.3. Combination of D_m and D_a

The m_p of a particle can be derived from its D_a and D_m, as shown in Eqs. (6) and (7):

$$\frac{D_m}{C_c(D_m)} = \frac{D_{ve}}{C_c(D_{ve})}\chi, \tag{6}$$

$$D_a{}^2 C_c(D_a) = \frac{D_{ve}{}^2 \rho_p C_c(D_{ve})}{\chi \cdot \rho_0}, \tag{7}$$

where $C_c(D)$ is the Cunningham slip correction factor, introduced to account for the reduction in drag that occurs when the relative velocity of the gas at the particle surface is nonzero (Peng and Bi, 2020). Combining Eqs. (6) and (7), the relationship between m_p and the diameters of D_a and D_m is represented by Eq. (8):

$$\frac{\pi D_m}{6C_c(D_m)}\rho_0 D_a{}^2 C_c(D_a) = \frac{\pi D_{ve}{}^3 \rho_p}{6} = m_p. \tag{8}$$

According to Eqs. (1) and (8), the ρ_e^I of a particle can be thus calculated using Eq. (9):

$$\rho_e^I = \frac{\rho_0 D_a^2 C_c(D_a)}{D_m^2 C_c(D_m)}. \quad (9)$$

Tavakoli and Olfert (2014) used this approach to obtain size-resolved ρ_e^I using a tandem setup consisting of an AAC and a SMPS (Fig. S2). In this setup, the AAC classifies the monodisperse particles with a specific D_a and the SMPS obtains the D_m of the monodisperse particles, which was used to measure the ρ_e^I of dioctyl sebacate (DOS) and soot particles. Fig. 4 shows that the measured ρ_e^I of DOS particles was 0.903 ± 0.90 g cm^{-3} and decreased to 0.86 ± 0.08 g cm^{-3} at 95 nm to 0.18 ± 0.02 g cm^{-3} at 637 nm for soot particles. Although the AAC-SMPS method is somewhat different from the CPMA-SMPS method, the advantages and disadvantages of these two methods when quantifying ρ_e^I are broadly the same. This is partly because both an AAC and CPMA are very accurate at characterising D_a and m_p, respectively. Specifically, an AAC does not require particles to be charged, which results in higher transmission efficiency in the AAC-SMPS and makes this setup more suitable for particles with multiple charges.

A tandem system combining a DMA with an electrical low-pressure impactor (ELPI) has also been used to measure ρ_e^I (Deye et al., 2012; Keskinen et al., 2011; Mamakos et al., 2013; Maricq, 2007; Maricq and Ning, 2004; Ristimaki and Keskinen, 2006). Briefly, particles are first classified using the DMA with a specific D_m and then the classified particles are transmitted into the ELPI, which segregates the particles according to their D_a and detects the electrical currents resulting from the charge of the deposited particles, which corresponds to the D_a size distribution. Based on this principle, Rostedt et al. (2009) and Juuti et al. (2016) developed an integrated instrument containing a charger, a zeroth-order mobility analyser, and an ELPI to measure ρ_e^I. This technique has an error in the order of ~10%, which mainly results from data scatter (3%), D_a measurement (6%), and the correction for multiply charged particles (Maricq and Ning, 2004). The DMA-ELPI setup has also been applied to measure the ρ_e^I of combustion aerosols produced by a mini-CAST burner operated under different conditions (Mamakos et al., 2013). Table S3 presents the operating conditions of the mini-CAST, and Fig. 5 shows that ρ_e^I decreased with an increase in D_m. However, the operating conditions strongly affected the ρ_e^I values, with ρ_e^I varying from 0.9 g cm^{-3} at condition 5 to 0.3 g cm^{-3} at condition 3 at 85 nm, for example.

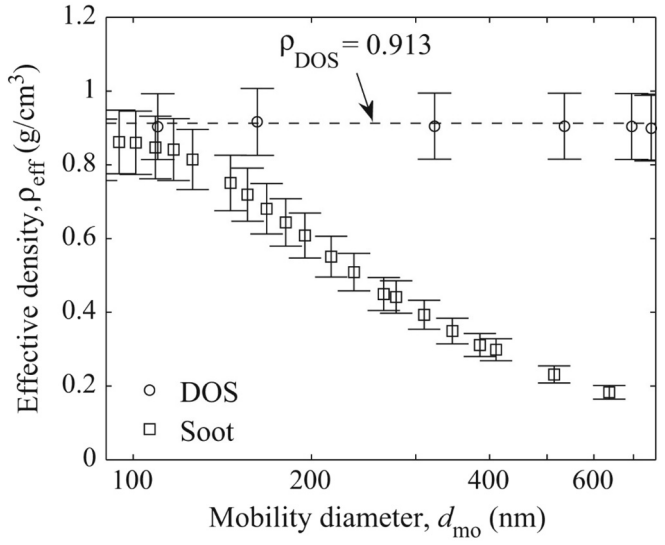

Fig. 4. ρ_e^I of soot and DOS particles.
Reprint with permission by Tavakoli and Olfert (2014).

Hyun et al. (2015) presented a modified setup consisting of a DMA and a single-stage low-pressure impactor (SELPI) to obtain D_m and D_a. The difference between the DMA-ELPI and DMA-SELPI setup is that the D_a of the particles in the latter case is obtained through the relationship between D_a and the collection efficiency (η) of the SELPI. This relationship is quantified in advance using NaCl aerosols with a pre-defined D_m. An aerosol electrometer detects the current carried by the NaCl aerosols (with a known D_m from the DMA) in the downstream (I_{down}) and upstream (I_{up}) of the impactor. The D_a of the NaCl with different D_m can be calculated using Eq. (9) based on ρ_e^I and D_m. Finally, the D_a of the collection efficiency curve can be obtained using Eq. (10):

$$\eta = \frac{a_1}{1 + exp\left(-\frac{D_a - D_{50}}{b}\right)} + a_2, \quad (10)$$

where D_{50} represents the cut-point or separation point, b represents the width of the fitting of the Boltzmann sigmoidal function, and a_1 and a_2 are coefficients. The D_a of the particles can be calculated from the curve when the efficiency of the aerosol is obtained. The DMA-SELPI setup was used to estimate the ρ_e^I of diesel exhaust particles, with ρ_e^I decreasing from 1.06 g cm^{-3} at 60 nm to 0.51 g cm^{-3} at 105 nm (Hyun et al., 2015). Note that currently only NaCl is used to determine the relationship between D_a and η, which may lead to uncertainty for other particle types with different characteristics.

The methods using the ELPI have a key disadvantage in that the measurement of D_a is affected by multiple charges. Two approaches have been applied to minimise these effects. The first approach uses an additional SMPS to obtain the size distribution for the classified particles, and thus the effects of multiply charged particles on the ELPI can be estimated (Deye et al., 2012; Ristimaki and Keskinen, 2006). The second approach is to correct the multiply charged particles from the DMA according to the relative population of multiply to singly charged particles (Keskinen et al., 2011; Mamakos et al., 2013; Maricq, 2007; Maricq and Ning, 2004).

Additionally, measuring D_m and D_a in parallel can determine ρ_e^I by fitting size distribution curves (Beddows et al., 2010; Kassianov et al., 2014; Khlystov et al., 2004; Zhao et al., 2017). The number distribution as a function of D_m can be measured using a SMPS or FMPS; however, the procedure of fitting to obtain the ρ_e^I is different because there are multiple ways of determining particle size distribution based on D_a. First, D_a can be obtained using an aerodynamic particle sizer (APS) (Beddows et al., 2010; Kassianov et al., 2014; Khlystov et al., 2004; Zhao et al., 2017). Studies using this method convert the D_a size distribution from APS data to the mobility spectrum by deriving a size correction factor (X) that gives the best least-squares fit with the SMPS data in the overlapping size range 542–680 nm, where X has the relationship with ρ_e^I shown in Eq. (11):

$$X = \sqrt{\rho_e^I}. \quad (11)$$

This approach was applied to derive the ρ_e^I of ambient particles on Marylebone Road, London, yielding values of 1.44 ± 0.39 g cm^{-3}.

Second, D_a can be obtained using an ELPI (Cha and Olofsson, 2018b; Nosko and Olofsson, 2017; Stein et al., 2013; Virtanen et al., 2004). In this case, ρ_e^I is obtained by minimising the mean error square between the D_a size distribution $dN_{ELPI}/d\log(D_a)$ and the D_m size distribution $dN_{SMPS}/d\log(D_m)$. Before the fitting process, the D_m size distribution columns of $dN_{SMPS}/d\log(D_m)$ are first adjusted into $dN_{SMPS}/d\log(D_a)$ based on Eq. (12). For j_1, $D_m > D_{a1}(\rho_e)$, and for j_2, $D_m \le D_{a2}(\rho_e)$, as follows:

$$\frac{dN_{SMPS}}{d\log D_a} = \frac{\sum_{j_1}^{j_2} dN_{SMPS}(D_{mj})}{\log(D_{a2}(\rho_e)) - \log(D_{a1}(\rho_e))}, \quad (12)$$

where D_{a2} is the maximum and D_{a1} is the minimum D_a of one ELPI channel. The ρ_e^I of particles in a railway tunnel with traffic was

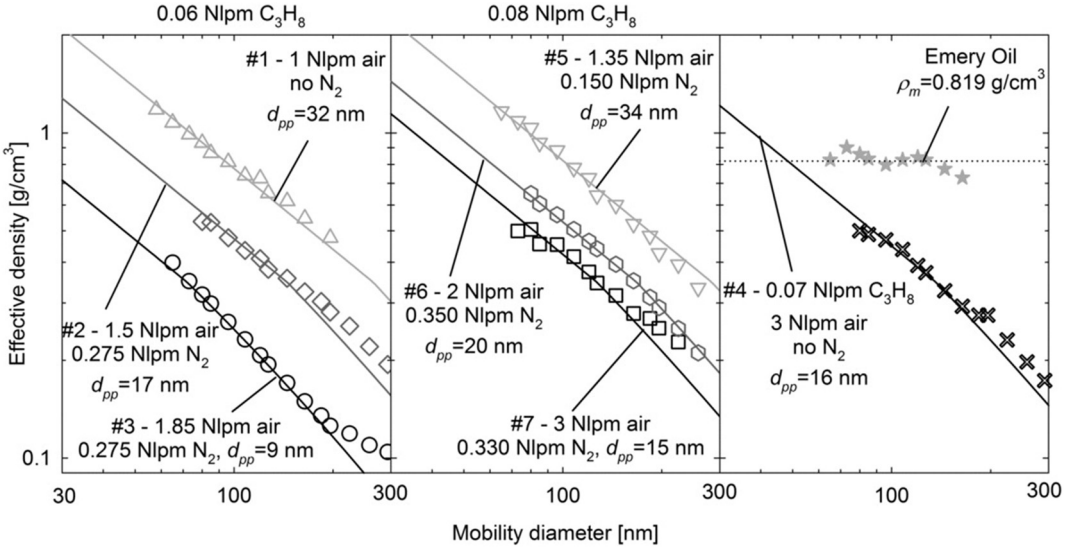

Fig. 5. Measured ρ_e^l of emery oil (star symbols) and different mini-CAST particles. Reprint with permission by (Mamakos et al., 2013).

determined to be 1.45 g cm^{-3} using the FMPS-ELPI setup compared to 1.64 g cm^{-3} without traffic using a ELPI-SMPS setup (Cha and Olofsson, 2018a). This indicates the potential of ρ_e^l to reflect different particle sources.

The third approach is a cascade epiphaniometer (CEPI) that measures Fuchs surface-area distributions as a function of D_a (S_f^{CEPI}) (Gini et al., 2016). In this case, the SMPS-measured number distributions are converted to surface-area distributions as a function of mobility diameters (S_f^{SMPS}) using Eq. (13):

$$S_f^{SMPS}(D_m) = N_{D_m}\frac{12\pi^2}{8.39\xi}\frac{\lambda_g D_m}{C_c(Kn)}, \tag{13}$$

where $\xi = 1.36$ (a dimensionless momentum scattering coefficient) (Zhang et al., 2012), λ_g is the gas mean free path, Kn is the particle Knudsen number ($Kn = 2\lambda_g/D_m$), and $C_c(Kn)$ is the corresponding Cunningham slip correction factor. N_{Dm} is the number concentration in each size bin, which is measured by the SMPS. The optimum ρ_e^l is determined by minimising the difference between S_f^{CEPI} and S_f^{SMPS} using the Nelder–Mead simplex algorithm. Optimisation can be implemented in MATLAB via the nonlinear curve- and data-fitting function 'lsqcurvefit' (available in the 'Optimization Toolbox'). The uncertainty of this technique was estimated to be <20% by Gini et al. (2016), who also found that the ρ_e^l of arbitrarily shaped carbon nanoparticles decreased from 1.31 g cm^{-3} to 0.35 g cm^{-3} as the geometric mean diameter increased.

Compared with the method of obtaining D_m and D_a in a tandem system, the major advantage of parallel measurement is that the system error caused by multiple charges can be eliminated and it simultaneously obtains two size distributions for the particles. However, parallel observation has a significant disadvantage in that ρ_e^l is derived from the relatively narrow particle size range of 542–680 nm. Therefore, large errors might be introduced when the derived ρ_e^l is used for aerosols across the entire analysed size range (up to 10,000 nm) because ρ_e^l varies with particle size.

2.4. (VT)DMA-SP2

A single particle soot photometer (SP2) is a powerful instrument that can quantify the microphysical properties of refractory black carbon (rBC) particles (Moteki and Kondo, 2007). Based on soot m_p directly measured using a SP2, the ρ_e^l of particles mixed with soot can be obtained in combination with a (volatility) tandem differential mobility analyser ((VT)DMA). Zhang et al. (2016b) first applied a VTDMA-SP2 setup (Fig. S3) for the in situ measurement of size-resolved ρ_e^l for ambient In-BC (i.e., internally mixed BC) cores. Using this approach, the monodisperse particles are selected by the first DMA (DMA1) and passed through a thermodenuder at 300 °C, where the In-BC size significantly decreases because of the evaporation of the coatings. Finally, the D_m and m_p of the In-BC cores are measured by a SMPS and a SP2, respectively. The ρ_e^l of an In-BC core measured using the VTDMA-SP2 setup is subject to at least 10% uncertainty because the coatings may not be completely removed by the thermodenuder, and the morphology of an In-BC core may change during the thermodenuder (Zhang et al., 2016b). Zhang et al. (2016b) used their VTDMA-SP2 at the Xianghe Atmospheric Observatory, China, to determine the ρ_e^l of an In-BC core, finding that values increased with the aging degree along with the compactness of the core, with an average value of 1.2 g cm^{-3}.

Wu et al. (2019) characterized ρ_e^l for Ex-BC particles using a tandem setup of a DMA and a SP2 (DMA-SP2). If a BC-containing particle is coated with nonrefractory components, the coating will evaporate before the rBC core incandesces, leading to a time lag between the incandescence peaks and scattering signals that are synchronously detected by the SP2. Thus, BC-containing particles with delay times shorter than 2 μs are identified as Ex-BC (i.e., externally mixed BC). According to D_m and m_p, the ρ_e^l of the Ex-BC particles can be calculated using Eq. (1). The uncertainty of this technique was not assessed by Wu et al. (2019) but is expected to be very low as long as the Ex-BC coatings have little effect on the particle size. The Ex-BC particles in the atmosphere of Beijing were measured to have ρ_e^l values decreasing from 0.46 g cm^{-3} at 140 nm to 0.14 g cm^{-3} at 750 nm (Wu et al., 2019).

Furthermore, Han et al. (2019) used the same setup (DMA-SP2) to determine the ρ_e^l of rBC-containing particles. In this case, the rBC core mass is first measured by the SP2, and the mass equivalent diameter (D_{me}) of the rBC core can be calculated as:

$$D_{me} = \sqrt[3]{\frac{6m_p}{\pi\rho}}, \tag{14}$$

where D_{me} is the diameter of a sphere containing the same mass of rBC as measured in the particle, and ρ is the material density of the rBC, which is 1.8 g cm^{-3}. Second, the optical diameter (D_o) of the particles is determined from the SP2 scattering signal amplitudes from rBC-

containing particles through a leading-edge-only fitting method. Third, the coating mass can be determined as $\rho_{coatings}\pi((D_o)^3 - (D_{me})^3)/6$, where $\rho_{coatings}$ is the ρ of the coating and is taken as 1.3 g cm^{-3}. Finally, ρ_e^I is determined based on m_p, the sum of the rBC core and coating masses, and the D_m of the rBC-containing particles, according to Eq. (1). Values of ρ_e^I for the fresh rBC-containing particles emitted from a diesel truck are shown in Fig. 6, decreasing from 1.97 ± 0.33 g cm^{-3} at 125 nm to 0.77 ± 0.13 g cm^{-3} at 300 nm, suggesting that larger BC aggregates are more fractal than smaller BC aggregates (Han et al., 2019).

The mixing state and ρ_e^I affect the optical properties of BC (Peng et al., 2016). Therefore, it is important to accurately characterise these physical properties. Compared to methods that cannot distinguish chemical composition, the ability to measure size-resolved ρ_e^I for BC particles is the greatest advantage of the SP2 method. The method developed by Zhang et al. (2016b) could be used to detect ρ_e^I for In-BC cores, whereas Wu et al. (2019) approach is capable of obtaining ρ_e^I for Ex-BC particles. These two methods have notable limitations in field observations because both In-BC and Ex-BC wildly coexist in the atmosphere.

While the method established by Han et al. (2019) can characterise the ρ_e^I of BC in different mixed states, there are notable shortcomings. First, it is not appropriate to set the ρ_p of the coating materials at a constant value of 1.3 g cm^{-3}. Second, uncertainty may exist in the calculation of the coating volume based on the assumption that the physical quantity D_o is identical to D_{me}. It should be noted that a slight difference between the diameters may lead to large biases when calculating the coating volume. However, Han et al. (2019) did not demonstrate an equivalent relationship between D_o and D_{me}. Therefore, although this method is a powerful technique, its accuracy may need to be further verified and improved.

3. Methods for the measurement of ρ_e^{II}

ρ_e^{II} can be characterized by the concurrent measurement of particle D_m and D_{va}, as shown in Eq. (2). The first technique involves coupling a DMA with an on-line aerosol mass spectrometer including single-particle mass spectrometer I and II (SPLAT I/II) (Alexander et al., 2016; Zelenyuk et al., 2005; Zelenyuk et al., 2006; Zelenyuk et al., 2008a; Zelenyuk et al., 2014; Zelenyuk et al., 2017; Zelenyuk et al., 2008b; Zelenyuk et al., 2008c), an aerosol mass spectrometer (AMS) (Dinar et al., 2006; Kiselev et al., 2010; Schneider et al., 2006), an aerosol time-of-flight mass spectrometer (ATOFMS) (Spencer and Prather, 2006; Spencer et al., 2007), and single-particle aerosol mass spectrometry (SPAMS) (Zhai et al., 2017; Zhang et al., 2016a). The second approach employs the parallel measurement of the volume distributions of the particles by SMPS and the mass distributions of the particles using an AMS.

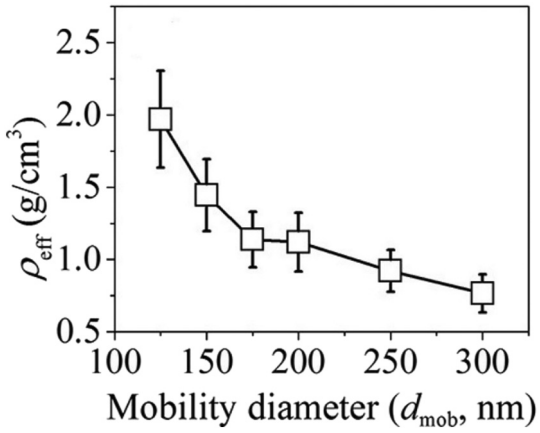

Fig. 6. ρ_e^I of rBC-containing particles as a function of D_m.
Reprint with permission by Han et al. (2019). Copyright 2019 American Chemical Society.

The tandem setup first classifies the particles with a specific D_m using the DMA and then measures the D_{va} and chemical composition of the classified particles (Fig. S4). The principles of all aerosol mass spectrometers for characterising D_{va} are similar, based on the flight time of the particles between two lasers. The particles classified by the DMA enter the mass spectrometer through an orifice and then pass through an aerodynamic lens at a velocity defined by their aerodynamic diameter. The flight time is obtained in a vacuum sizing area, which can be transformed into D_{va} using a calibration curve. The calibration curve is obtained by fitting PSL with sizes from 100 nm to 2000 nm to their flight times before the measurement. Combining chemical composition information and the diameters D_{va} and D_m, the tandem setup can obtain the chemically resolved ρ_e^{II} of the sampled particles. Fig. 7 shows three distinct D_{va} modes at 120, 390, and 420 nm, and the number fraction of different chemical classes at each mode for atmospheric particles with a D_m of 450 nm. The results show that EC, Ca-EC-Sulphate (produced by lubricating oil), and aged organic carbon particles are the main components of particles with ρ_e^{II} values of ~0.27, 0.87, and 0.93 g cm^{-3}, respectively (Spencer et al., 2007).

The greatest advantage of this technique is that the mass spectrometer can determine the chemical composition of particles and, therefore, can chemically resolve ρ_e^{II}. Thus, the DMA-mass spectrometer can accurately measure size-resolved and chemically resolved ρ_e^{II}. However, it has the disadvantage of being unable to characterise ρ_e^{II} for particles with $\rho_e^{II} \cdot D_m/\rho_0$ values less than 100 nm (Su et al., 2004). For example, this method cannot accurately determine the ρ_e^{II} of BC particles with a D_m smaller than 250 nm when ρ_e^{II} is equal to or less than 0.4 g cm^{-3}. In addition, the influence of the multiple charges must be considered during the calculation of ρ_e^{II}.

The parallel technique consisting of a SMPS and a AMS has been used to estimate ρ_e^{II} (Alfarra et al., 2006; Bahreini et al., 2005; Hao et al., 2009; Murphy et al., 2009; Poulain et al., 2010; Saathoff et al., 2009; Slowik et al., 2007; Slowik et al., 2004; Varutbangkul et al., 2006). The former instrument measures the particle D_m number distribution, which is converted into a volume distribution. The latter instrument measures the particle mass concentration and D_{va}, which are expressed as the mass distribution. The volume distribution versus D_m, and the mass distribution versus D_{va}, are then fitted by the log-normal distribution. Interpolation is then employed to account for SMPS and AMS machines with different time resolutions. Finally, D_m and D_{va} are obtained from the mode diameters of the two fitted distributions, respectively, which are used to calculate ρ_e^{II} using Eq. (2). For example, Murphy et al. (2009) applied this setup to measure the ρ_e^{II} of the wet particles emitted from a ship, obtaining a value of 1.4 g cm^{-3}.

Compared with the tandem system, the parallel method can provide more information including the size distributions for D_m and D_{va} as well as mass distribution. However, this technique has three key limitations. First, it requires mass spectrometry with the ability to quantitatively measure the mass concentration of particles, which excludes the application of single-particle mass spectrometry, such as SPLAT I and II, ATOFMS, and SPAMS. Second, ρ_e^{II} can only be obtained when the two volume distributions are fitted into unimodal distributions, which restricts the measurement of ρ_e^{II} for aerosols with complicated compositions. Finally, ρ_e^{II} obtained using this method represents the average ρ_e of multiple sizes, the accuracy of which requires further evaluation.

4. Methods for the measurement of ρ_e^{III}

ρ_e^{III} can be retrieved from a fitting procedure that compares the measured light-scattering intensity of particles to their theoretical values. An ATOFMS has the ability to capture single-particle light scattering

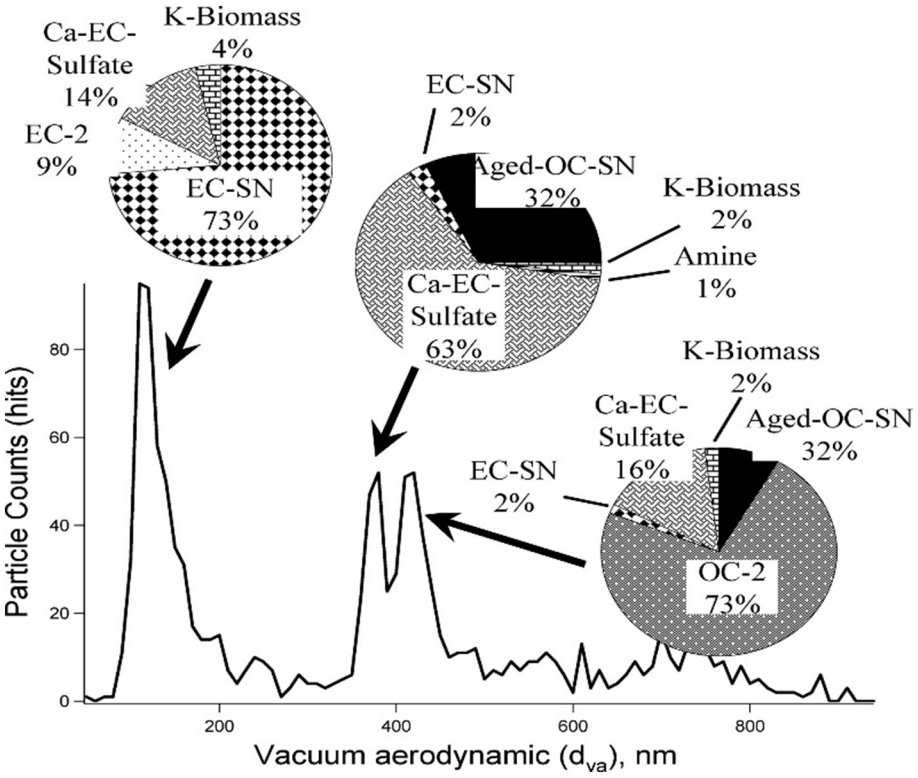

Fig. 7. D_{va} size distribution of ambient particles with a D_m of 450 nm.
Reprint with permission by Spencer et al. (2007). Copyright 2007 American Chemical Society.

signals, and the theoretical light-scattering cross section can be calculated using the following equation:

$$R_{theory} = \frac{1}{k^2}\iint\left(|S_1|^2\sin^2\phi + |S_2|^2\cos^2\phi\right)\sin\theta d\theta d\phi, \quad (15)$$

where k is the wavenumber, $k = 2\pi/\lambda$ (λ is the wavelength of light), φ is the azimuth angle from the plane of polarisation, θ is the polar angle, and S_1 and S_2 are the scattering amplitude matrix elements. S_1 and S_2 are calculated using Mie theory and as a function of the refractive index, expressed as the real refractive index n for scattering calculation, and D_{ve}, λ, and θ. The refractive index is given by $l = n + i \times k$, where n and k are constants and $i = (-1)^{1/2}$. The relationship between D_{va} and D_{ve} is expressed in Eq. (16):

$$D_{va} = \frac{\rho_p}{\rho_0}\frac{D_{ve}}{\chi_v} = D_{ve}\frac{\rho_e^{III}}{\rho_0}, \quad (16)$$

and R_{theory} can be expressed as a function of n and ρ_e^{III}. The measured single-particle light scattering signal (R_{meas}) can be converted to R_{theory} through a calibration function derived by fitting the R_{meas} for PSL particles with a series of known sizes to their R_{theory}, calculated using Eq. (15). To retrieve n and ρ_e^{III}, a series of n and ρ_e^{III} values are used as the inputs in Eq. (15) to calculate the $R_{theory,test,}$ and determine the best fit between R_{theory} and $R_{theory,test}$ based on the least square method, thus enabling the estimation of n and ρ_e^{III}.

Because the Mie theory used in the calculation of S_1 and S_2 is only applicable to spherical particles, an ATOFMS can theoretically obtain ρ_e^{III} for spherical particles. Moffet and Prather (2005) first derived the ρ_e^{III} of PSL and dioctyl sebacate (DOS) particles using an ATOFMS, which were broadly equal to the ρ of the spherical particles. Murphy et al. (2009) applied this method to estimate the ρ_e^{III} of ambient particles in Mexico City, finding that the density of particles with different chemical compositions ranged from 1.1 to 3.4 g cm^{-3}. However, the errors of the density determinations were as high as 20%, mainly as a result of not considering the influence of particle size on light scattering during the retrieval processes.

For non-spherical particles, Moffet et al. (2008) and Zhang et al. (2016a) applied an ATOFMS and SPAMS to obtain ρ_e^{III}, respectively. However, Moffet et al. (2008) failed to fit the $R_{theory,test}$ well to R_{theory} for dry NaCl particles and calcium-rich dust. Zhang et al. (2016a) also failed to simultaneously retrieve ρ_e^{III} and n for $(NH_4)_2SO_4$ and $NaNO_3$. Therefore, this method can characterise ρ_e^{III} for spherical particles but not non-spherical particles, which greatly limits its application.

5. Summary

ρ_e, as an alternative to ρ_p, is one of the important physical properties of aerosols that must be determined in environmental and human health studies. This review has summarised the currently available techniques to derive ρ_e using three different approaches. While these techniques have proved valuable in understanding aerosol ρ_e, further work is needed to facilitate further in-depth research.

Table 2 summarises the key features and advantages and disadvantages of the methods discussed for determining aerosol ρ_e. The chemical composition of particles are not available for the first four methods, applied in the measurement of ρ_e^I, as listed in Table 2a. Additional valuable information, such as mass concentration and size distribution, can be obtained by the methods of combining C_M and C_V and measuring D_m and D_a in parallel, although size-resolved ρ_e^I is unavailable. Differently, methods for measuring m_p/D_a and D_m in tandem can accurately determine size-resolved ρ_e^I.

Table 2b shows the four methods employed for obtaining chemical-resolved ρ_e. Unfortunately, the SMPS-AMS setup only obtains ρ_e^{II} at a specific size, and the ATOFMS/SPAMS setup cannot be applied to non-spherical particles, indicating that improvements are still required. The ability to measure the size-resolved ρ_e of particles with specific or variable chemical components should be the focus of future development. DMA-SP2 and tandem DMA-mass spectrometers are currently the most powerful methods, which have great potential for further

Table 2
Summary and comparison of several features of methods for aerosol effective density measurement.

(a)

Methods	C_M and C_V	D_m and D_a in parallel	D_m and m_p	D_m and D_a in tandem
1) Type of ρ_e	ρ_e^I	ρ_e^I	ρ_e^I	ρ_e^I
2) Assumption/preset	ρ_e^I is 1.5 g cm^{-3}	ρ_e is independent with size	No	No
3) Chemical resolution	No	No	No	No
4) Size range	A few to thousands nm	Not applicable	$< D_m$ 1 μm	$< D_m$ 1 μm
5) Size resolution	No	No	Yes	Yes
6) Deviation	9–17% for SMPS-QCM	< 20% for SMPS-CEPI	< 5%	< 5% or ~10% for DMA-ELPI

(b)

Methods	SMPS-AMS	ATOFMS/SPAMS	DMA-SP2	DMA-mass spectrometer
1) Type of ρ_e	ρ_e^{II}	ρ_e^{III}	ρ_e^I	ρ_e^{II}
2) Assumption/preset	No	Particle is spherical	$\rho_{coatings}$ is 1.3 g cm^{-3}	No
3) Chemical resolution	Yes	Yes	Yes	Yes
4) Size range	Not applicable	$> D_{va}$ 100 nm	$< D_m$ 1 μm	Hundreds nm to 1 μm
5) Size resolution	No	No	Yes	Yes
6) Deviation	Not applicable	< 5%	Not applicable	< 5%

improvement. The (*VT*)DMA-SP2 setup is specifically applied to BC particles and is capable of measuring the ρ_e^I for In-BC cores and Ex-BC. However, this method is not accurate enough to simultaneously obtain ρ_e^I for BC particles with differing mixing states through the introduction of D_o. Therefore, determining the relationship between D_o and D_{me} should help establish the DMA-SP2 approach as a more powerful method. A DMA-mass spectrometer has the distinctive characteristics of high accuracy and chemical composition resolution for the measurement of ρ_e^{II}. However, the applicability of this is limited by the size measurement capability of the mass spectrometer. As suggested by McMurry et al. (2002), aerosol measurement should ideally determine the complete chemistry of single particles and other microphysical properties (e.g., densities, refractive indices, volatilities, and hygroscopicities) with continuous size and time resolutions. Therefore, we suggest that further improvements in particle density technology should focus on the measurement of particles using aerosol mass spectrometers across a wide size range coupled with the measurements of other key properties. Establishing the link between particle density and other properties might help validate the assumptions of particle density in models aimed at predicting the impacts of aerosols (Koch et al., 2009).

Declaration of competing interest

The authors declare that they have no known competing financial interests or personal relationships that could have appeared to influence the work reported in this paper.

Acknowledgements

This work was supported by the National Natural Science Foundation of China (Grant Nos. 41775124 and 41877307), the Natural Science Foundation of Guangdong Province (2019B151502022), and Guangdong Foundation for Program of Science and Technology Research (Grant Nos. 2019B121205006 and 2017B030314057). This is contribution No.IS-2994 from CASGIG.

Appendix A

Table A1
Symbols used in this paper.

Symbol	Meaning	Symbol	Meaning
a_1 and a_2	Coefficients	b	Width of fitting
C_M	Mass concentration	C_{BC}	Mass concentration of BC-core
C_V	Volume concentration	$C_c\,(D)$	Cunningham slip correction factor
D_{50}	Cutpoint point	D_{a1} and D_{a2}	Minimum and Maximum D_a
D_a	Aerodynamic diameter	D_{va}	Vacuum aerodynamic diameter
D_m	Mobility diameter	D_{ve}	Volume equivalent diameter
D_{me}	Mass equivalent diameter	D_o	Optical diameter
I_{down}	Downstream current	I_{up}	Upstream current
k	Wavenumber	Kn	Knudsen number
m_p	Particle mass	l	Refractive index
n	Real refractive index	N_{Dm}	Number concentration
ρ	Density	$\rho_{coatings}$	Density of coating
ρ_0	Unit density	ρ_e	Effective density
ρ_p	Particle density	ρ_e^I, ρ_e^{II}, and ρ_e^{III}	Three definitions of ρ_e
ρ_m	Material density	V_a	Apparent volume
V	Volume	R_{theory} *and* R_{meas}	Theoretical light scattering signal
X	Size correction factor	R_{meas}	Measured light scattering signal
χ	Dynamic shape factor	$R_{theory,test,}$	R_{theory} calculated by n and ρ_e
η	Collection efficiency	S_1 and S_2	Scattering amplitude matrix elements
ξ	Scattering coefficient	S_f^{CEPI} and S_f^{SMPS}	D_a and D_m surface-area distributions
λ	Wavelength of the light	φ	Azimuth angle
λ_g	Gas mean free path	θ	Polar angle
e	Elementary charge	Q_a	Aerosol flow
N	The number of charges	Q_{sh}	Sheath flow
μ	Gas viscosity	V_o	Voltage
ω	Rotational speed	L	Rod length
R_1	Inner cylinder radius	R_3	Inner radius
R_2	Outer cylinder radius	R_4	Outer radius

Appendix B

Table B1
Introductions of the diameters used in this paper.

Diameter	Definition	Derivation	Application
D_{ve}	The diameter of a spherical particle of the same volume, including the voids in the particles, as the particle under consideration	$D_{ve} = \sqrt[3]{\frac{6m_p}{\pi\rho_p}}$	As a reference
D_{me}	The diameter of a spherical particle of the same volume, excluding the voids in the particles, as the particle under consideration	$D_{me} = \sqrt[3]{\frac{6m_p}{\pi\rho_m}}$	As a reference
D_a	The diameter of a sphere with standard density that settles at the same terminal velocity as the particle of interest	$D_a = D_{ve}\sqrt{\frac{\rho_p C_c(D_{ve})}{\chi\rho_0 C_c(D_a)}}$	AAC, APS, ELPI, LAS-X

Table B1 (*continued*)

Diameter	Definition	Derivation	Application
D_{va}	The D_a in the free-molecular regime	$D_{va} = \frac{\rho_p}{\rho_0}\frac{D_{ve}}{\chi}$	AMS, SPLAT, ATOFMS, SPAMS
D_m	The diameter of a sphere with the same migration velocity in a constant electric field as the particle of interest	$\frac{D_m}{C_c(D_m)} = \frac{D_{ve}}{C_c(D_{ve})}\chi$	DMA

Appendix C. Supplementary data

Supplementary data to this article can be found online at https://doi.org/10.1016/j.scitotenv.2021.146248.

References

Alexander, J.M., Bell, D.M., Imre, D., Kleiber, P.D., Grassian, V.H., Zelenyuk, A., 2016. Measurement of size-dependent dynamic shape factors of quartz particles in two flow regimes. Aerosol Sci. Technol. 50, 870–879. https://doi.org/10.1080/02786826.2016.1200006.

Alfarra, M.R., Paulsen, D., Gysel, M., Garforth, A.A., Dommen, J., Prevot, A.S.H., Worsnop, D.R., Baltensperger, U., Coe, H., 2006. A mass spectrometric study of secondary organic aerosols formed from the photooxidation of anthropogenic and biogenic precursors in a reaction chamber. Atmos. Chem. Phys. 6, 5279–5293. https://doi.org/10.5194/acp-6-5279-2006.

Bahreini, R., Keywood, M.D., Ng, N.L., Varutbangkul, V., Gao, S., Flagan, R.C., Seinfeld, J.H., Worsnop, D.R., Jimenez, J.L., 2005. Measurements of secondary organic aerosol from oxidation of cycloalkenes, terpenes, and m-xylene using an aerodyne aerosol mass spectrometer. Environ. Sci. Technol. 39, 5674–5688. https://doi.org/10.1021/es048061a.

Beddows, D.C.S., Dall'osto, M., Harrison, R.M., 2010. An enhanced procedure for the merging of atmospheric particle size distribution data measured using electrical mobility and time-of-flight analysers. Aerosol Sci. Technol. 44, 930–938. https://doi.org/10.1080/02786826.2010.502159.

Brossell, D., Valenti, M., Bezantakos, S., Schmidt-Ott, A., Biskos, G., 2015. The nano-particle mass classifier (Nano-PMC): development, characterization, and application for determining the mass, apparent density, and shape of particles with masses down to the zeptogram range. Aerosol Sci. Technol. 49, 495–507.

Bullock, D.S., Olfert, J.S., 2014. Size, volatility, and effective density of particulate emissions from a homogeneous charge compression ignition engine using compressed natural gas. J. Aerosol Sci. 75, 1–8. https://doi.org/10.1016/j.jaerosci.2014.04.005.

Buseck, P.R., Posfai, M., 1999. Airborne minerals and related aerosol particles: effects on climate and the environment. Proc. Natl. Acad. Sci. U. S. A. 96, 3372–3379. https://doi.org/10.1073/pnas.96.7.3372.

Cha, Y., Olofsson, U., 2018a. Effective density of airborne particles in a railway tunnel from field measurements of mobility and aerodynamic size distributions. Aerosol Sci. Technol. 52, 886–899. https://doi.org/10.1080/02786826.2018.1476750.

Cha, Y.Y., Olofsson, U., 2018b. Effective density of airborne particles in a railway tunnel from field measurements of mobility and aerodynamic size distributions. Aerosol Sci. Technol. 52, 886–899.

Cross, E.S., Slowik, J.G., Davidovits, P., Allan, J.D., Worsnop, D.R., Jayne, J.T., Lewis, D.K., Canagaratna, M., Onasch, T.B., 2007. Laboratory and ambient particle density determinations using light scattering in conjunction with aerosol mass spectrometry. Aerosol Sci. Technol. 41, 343–359. https://doi.org/10.1080/02786820701199736.

Dastanpour, R., Momenimovahed, A., Thomson, K., Olfert, J., Rogak, S., 2017. Variation of the optical properties of soot as a function of particle mass. Carbon 124, 201–211. https://doi.org/10.1016/j.carbon.2017.07.005.

DeCarlo, P.F., Slowik, J.G., Worsnop, D.R., Davidovits, P., Jimenez, J.L., 2004. Particle morphology and density characterization by combined mobility and aerodynamic diameter measurements. Part 1: theory. Aerosol Sci. Technol. 38, 1185–1205.

Deye, G.J., Kulkarni, P., Ku, B.K., 2012. Morphological characterization of carbon nanofiber aerosol using tandem mobility and aerodynamic size measurements. J. Nanopart. Res. 14, 1112. https://doi.org/10.1007/S11051-012-1112-1.

Dinar, E., Mentel, T.F., Rudich, Y., 2006. The density of humic acids and humic like substances (HULIS) from fresh and aged wood burning and pollution aerosol particles. Atmos. Chem. Phys. 6, 5213–5224. https://doi.org/10.5194/acp-6-5213-2006.

Finlayson-Pitts, B.J., Pitts Jr., J.N., 1999. Chemistry of the Upper and Lower Atmosphere: Theory, Experiments, and Applications: Elsevier.

Fujitani, Y., Saitoh, K., Kondo, Y., Fushimi, A., Takami, A., Tanabe, K., Kobayashi, S., 2016. Characterization of structure of single particles from various automobile engines under steady-state conditions. Aerosol Sci. Technol. 50, 1055–1067.

Geller, M., Biswas, S., Sioutas, C., 2006. Determination of particle effective density in urban environments with a differential mobility analyzer and aerosol particle mass analyzer. Aerosol Sci. Technol. 40, 709–723. https://doi.org/10.1080/02786820600803925.

Gini, M.I., Helmis, C., Melas, A.D., Papanastasiou, D., Orfanopoulos, G., Giannakopoulos, K.P., Drossinos, Y., Eleftheriadis, K., 2016. Characterization of carbon fractal-like aggregates by size distribution measurements and theoretical calculations. Aerosol Sci. Technol. 50, 133–147. https://doi.org/10.1080/02786826.2015.1134763.

Guo, S., Hu, M., Zamora, M.L., Peng, J.F., Shang, D.J., Zheng, J., Du, Z.F., Wu, Z., Shao, M., Zeng, L.M., Molina, M.J., Zhang, R.Y., 2014. Elucidating severe urban haze formation in China. Proc. Natl. Acad. Sci. U. S. A. 111, 17373–17378.

Han C., Li S.M., Liu P., Lee P., 2019. Size dependence of the physical characteristics of particles containing refractory black carbon in diesel vehicle exhaust. Environ. Sci. Technol. 53, doi:137–145. https://doi.org/10.1021/acs.est.8b04603.

Hao, L.Q., Yli-Pirila, P., Tiitta, P., Romakkaniemi, S., Vaattovaara, P., Kajos, M.K., Rinne, J., Heijari, J., Kortelainen, A., Miettinen, P., Kroll, J.H., Holopainen, J.K., Smith, J.N., Joutsensaari, J., Kulmala, M., Worsnop, D.R., Laaksonen, A., 2009. New particle formation from the oxidation of direct emissions of pine seedlings. Atmos. Chem. Phys. 9, 8121–8137.

Hu, M., Peng, J.F., Sun, K., Yue, D.L., Guo, S., Wiedensohler, A., Wu, Z.J., 2012. Estimation of size-resolved ambient particle density based on the measurement of aerosol number, mass, and chemical size distributions in the winter in Beijing. Environ. Sci. Technol. 46, 9941–9947.

Hyun, J., Nasr, A.M., Choi, N.K., Park, D., Hwang, J., 2015. Design and performance test of a lab-made single-stage low-pressure impactor for morphology analysis of diesel exhaust particles. Aerosol Sci. Technol. 49, 895–901. https://doi.org/10.1080/02786826.2015.1081669.

Jeong, B., Lee, J., 2017. Effective density and light absorption cross section of black carbon generated in a spark discharger. J. Aerosol Sci. 107, 55–64. https://doi.org/10.1016/j.jaerosci.2017.02.007.

Johnson, T.J., Olfert, J.S., Cabot, R., Treacy, C., Yurteri, C.U., Dickens, C., McAughey, J., Symonds, J.P.R., 2015a. Transient measurement of the effective particle density of cigarette smoke. J. Aerosol Sci. 87, 63–74. https://doi.org/10.1016/j.jaerosci.2015.05.006.

Johnson, T.J., Olfert, J.S., Symonds, J.P.R., Johnson, M., Rindlisbacher, T., Swanson, J.J., Boies, A.M., Thomson, K., Smallwood, G., Walters, D., Sevcenco, Y., Crayford, A., Dastanpour, R., Rogak, S.N., Durdina, L., Bahk, Y.K., Brem, B., Wang, J., 2015b. Effective density and mass-mobility exponent of aircraft turbine particulate matter. J. Propuls. Power 31, 573–582. https://doi.org/10.2514/1.B35367.

Juuti, P., Arffman, A., Rostedt, A., Harra, J., Makela, J.M., Keskinen, J., 2016. Real-time effective density monitor (DENSMO) for aerosol nanoparticle production. Aerosol Sci. Technol. 50, 487–496. https://doi.org/10.1080/02786826.2016.1168511.

Kassianov, E., Barnard, J., Pekour, M., Berg, L.K., Shilling, J., Flynn, C., Mei, F., Jefferson, A., 2014. Simultaneous retrieval of effective refractive index and density from size distribution and light-scattering data: weakly absorbing aerosol. Atmos. Meas. Tech. 7, 3247–3261. https://doi.org/10.5194/amt-7-3247-2014.

Katrib Y., Martin S.T., Rudich Y., Davidovits P., Jayne J.T., Worsnop D.R., 2005. Density changes of aerosol particles as a result of chemical reaction. Atmos. Chem. Phys. 5, 275-291. DOI doi:https://doi.org/10.5194/acp-5-275-2005.

Kazemimanesh, M., Dastanpour, R., Baldelli, A., Moallemi, A., Thomson, K.A., Jefferson, M.A., Johnso, M.R., Rogak, S.N., Olfert, J.S., 2019. Size, effective density, morphology, and nano-structure of soot particles generated from buoyant turbulent diffusion flames. J. Aerosol Sci. 132, 22–31.

Keskinen, H., Romakkaniemi, S., Jaatinen, A., Miettinen, P., Saukko, E., Joutsensaari, J., Makela, J.M., Virtanen, A., Smith, J.N., Laaksonen, A., 2011. On-line characterization of morphology and water adsorption on fumed silica nanoparticles. Aerosol Sci. Technol. 45, 1441–1447.

Khlystov, A., Stanier, C., Pandis, S.N., 2004. An algorithm for combining electrical mobility and aerodynamic size distributions data when measuring ambient aerosol. Aerosol Sci. Technol. 38, 229–238. https://doi.org/10.1080/02786820390229543.

Kiselev, A., Wennrich, C., Stratmann, F., Wex, H., Henning, S., Mentel, T.F., Kiendler-Scharr, A., Schneider, J., Walter, S., Lieberwirth, I., 2010. Morphological characterization of soot aerosol particles during LACIS Experiment in November (LExNo). J. Geophys. Res. Atmos. 115, D11204. https://doi.org/10.1029/2009jd012635.

Koch, D., Schulz, M., Kinne, S., McNaughton, C., Spackman, J.R., Balkanski, Y., Bauer, S., Berntsen, T., Bond, T.C., Boucher, O., Chin, M., Clarke, A., De Luca, N., Dentener, F., Diehl, T., Dubovik, O., Easter, R., Fahey, D.W., Feichter, J., Fillmore, D., Freitag, S., Ghan, S., Ginoux, P., Gong, S., Horowitz, L., Iversen, T., Kirkev, Aring, G.A., Klimont, Z., Kondo, Y., Krol, M., Liu, X., Miller, R., Montanaro, V., Moteki, N., Myhre, G., Penner, J.E., Perlwitz, J., Pitari, G., Reddy, S., Sahu, L., Sakamoto, H., Schuster, G., Schwarz, J.P., Seland, Ø., Stier, P., Takegawa, N., Takemura, T., Textor, C., van Aardenne, J.A., Zhao, Y., 2009. Evaluation of black carbon estimations in global aerosol models. Atmos. Chem. Phys. 9, 9001–9026. https://doi.org/10.5194/acp-9-9001-2009.

Leskinen, J., Ihalainen, M., Torvela, T., Kortelainen, M., Lamberg, H., Tiitta, P., Jakobi, G., Grigonyte, J., Joutsensaari, J., Sippula, O., Tissari, J., Virtanen, A., Zimmermann, R., Jokiniemi, J., 2014. Effective density and morphology of particles emitted from small-scale combustion of various wood fuels. Environ. Sci. Technol. 48, 13298–13306. https://doi.org/10.1021/es502214a.

Levy, M.E., Zhang, R.Y., Zheng, J., Tan, H.B., Wang, Y., Molina, L.T., Takahama, S., Russell, L.M., Li, G.H., 2014. Measurements of submicron aerosols at the California-Mexico border during the Cal-Mex 2010 field campaign. Atmos. Environ. 88, 308–319. https://doi.org/10.1016/j.atmosenv.2013.08.062.

Li, C., Hu, Y., Chen, J., Ma, Z., Ye, X., Yang, X., Wang, L., Wang, X., Mellouki, A., 2016. Physiochemical properties of carbonaceous aerosol from agricultural residue burning: density, volatility, and hygroscopicity. Atmos. Environ. 140, 94–105. https://doi.org/10.1016/j.atmosenv.2016.05.052.

Lin, G.Y., Lee, G.R., Lin, S.F., Hung, Y.H., Li, S.W., Wu, G.J., Ye, H.J., Huang, W., Tsai, C.J., 2015. Ultrafine particles and pm2.5 at three urban air monitoring stations in northern Taiwan from 2011 to 2013. Aerosol Air Qual. Res. 15, 2305–2319. https://doi.org/10.4209/aaqr.2015.04.0271.

Lin Y., Bahreini R., Zimmerman S., Fofie E.A., Asa-Awuku A., Park K., Lee S.-B., Bae G.-N., Jung H.S., 2018. Investigation of ambient aerosol effective density with and without using a catalytic stripper. Atmos. Environ.187, 84-92. doi:https://doi.org/10.1016/j.atmosenv.2018.05.063.

Liu, Y., Daum, P.H., 2008. Relationship of refractive index to mass density and self-consistency of mixing rules for multicomponent mixtures like ambient aerosols. J. Aerosol Sci. 39, 974–986. https://doi.org/10.1016/j.jaerosci.2008.06.006.
Liu, Z., Hu, B., Ji, D., Wang, Y., Wang, M., Wang, Y., 2015. Diurnal and seasonal variation of the $PM_{2.5}$ apparent particle density in Beijing. China. Atmos. Environ. 120, 328–338. https://doi.org/10.1016/j.atmosenv.2015.09.005.
Ma Y., Li S.Z., Zheng J., Khalizov A., Wang X., Wang Z., Zhou Y.Y., 2017. Size-resolved measurements of mixing state and cloud-nucleating ability of aerosols in Nanjing, China. J. Geophys. Res.: Atmos. 122, 9430–9450. doi:https://doi.org/10.1002/2017JD026583.
Malik, A., Abdulhamid, H., Pagels, J., Rissler, J., Lindskog, M., Nilsson, P., Bjorklund, R., Jozsa, P., Visser, J., Spetz, A., Sanati, M., 2011. A potential soot mass determination method from resistivity measurement of thermophoretically deposited soot. Aerosol Sci. Technol. 45, 284–294.
Malloy, Q.G.J., Nakao, S., Qi, L., Austin, R., Stothers, C., Hagino, H., Cocker III, D.R., 2009. Real-time aerosol density determination utilizing a modified scanning mobility particle sizeraerosol particle mass analyzer system. Aerosol Sci. Technol. 43, 673–678. https://doi.org/10.1080/02786820902832960.
Mamakos, A., Khalek, I., Giannelli, R., Spears, M., 2013. Characterization of combustion aerosol produced by a mini-cast and treated in a catalytic stripper. Aerosol Sci. Technol. 47, 927–936.
Maricq, M.M., 2007. Coagulation dynamics of fractal-like soot aggregates. J. Aerosol Sci. 38, 141–156.
Maricq, M.M., Ning, X., 2004. The effective density and fractal dimension of soot particles from premixed flames and motor vehicle exhaust. J. Aerosol Sci. 35, 1251–1274. https://doi.org/10.1016/j.jaerosci.2004.05.002.
McMurry, P.H., Wang, X., Park, K., Ehara, K., 2002. The relationship between mass and mobility for atmospheric particles: A new technique for measuring particle density. Aerosol Sci. Technol. 36, 227–238. https://doi.org/10.1080/027868202753504083.
Moffet, R.C., Prather, K.A., 2005. Extending ATOFMS measurements to include refractive index and density. Anal. Chem. 77, 6535–6541. https://doi.org/10.1021/ac0503097.
Moffet, R.C., Qin, X.Y., Rebotier, T., Furutani, H., Prather, K.A., 2008. Chemically segregated optical and microphysical properties of ambient aerosols measured in a single-particle mass spectrometer. J. Geophys. Res. Atmos. 113, D12. https://doi.org/10.1029/2007jd009393.
Momenimovahed, A., Olfert, J.S., 2015. Effective density and volatility of particles emitted from gasoline direct injection vehicles and implications for particle mass measurement. Aerosol Sci. Technol. 49, 1051–1062. https://doi.org/10.1080/02786826.2015.1094181.
Morawska, L., Johnson, G., Ristovski, Z.D., Agranovski, V., 1999. Relation between particle mass and number for submicrometer airborne particles. Atmos. Environ. 33, 1983–1990.
Moteki, N., Kondo, Y., 2007. Effects of mixing state on black carbon measurements by laser-induced incandescence. Aerosol Sci. Technol. 41, 398–417.
Murphy, D.M., Cziczo, D.J., Hudson, P.K., Schein, M.E., Thomson, D.S., 2004. Particle density inferred from simultaneous optical and aerodynamic diameters sorted by composition. J. Aerosol Sci. 35, 135–139. https://doi.org/10.1016/s0021-8502(03)00386-0.
Murphy, S.M., Agrawal, H., Sorooshian, A., Padro, L.T., Gates, H., Hersey, S., Welch, W.A., Jung, H., Miller, J.W., Cocker, D.R., Nenes, A., Jonsson, H.H., Flagan, R.C., Seinfeld, J.H., 2009. Comprehensive simultaneous shipboard and airborne characterization of exhaust from a modern container ship at sea. Environ. Sci. Technol. 43, 4626–4640.
Nakagawa, M., Nakayama, T., Sasago, H., Ueda, S., Venables, D.S., Matsumi, Y., 2016. Design and characterization of a novel single-particle polar nephelometer. Aerosol Sci. Technol. 50, 392–404. https://doi.org/10.1080/02786826.2016.1155105.
Nakayama T., Ikeda Y., Sawada Y., Setoguchi Y., Ogawa S., Kawana K., Mochida M., Ikemori F., Matsumoto K., Matsumi Y., 2014. Properties of light-absorbing aerosols in the Nagoya urban area, Japan, in August 2011 and January 2012: Contributions of brown carbon and lensing effect. J. Geophys. Res.: Atmos. 119, 12721–12739. doi:https://doi.org/10.1002/2014JD021744.
Nosko, O., Olofsson, U., 2017. Effective density of airborne wear particles from car brake materials. J. Aerosol Sci. 107, 94–106. https://doi.org/10.1016/j.jaerosci.2017.02.014.
Olfert, J., Rogak, S., 2019. Universal relations between soot effective density and primary particle size for common combustion sources. Aerosol Sci. Technol. 53, 485–492.
Olfert, J.S., Collings, N., 2005. New method for particle mass classification - the Couette centrifugal particle mass analyzer. J. Aerosol Sci. 36, 1338–1352. https://doi.org/10.1016/j.jaerosci.2005.03.006.
Olfert, J.S., Symonds, J.P.R., Collings, N., 2007. The effective density and fractal dimension of particles emitted from a light-duty diesel vehicle with a diesel oxidation catalyst. J. Aerosol Sci. 38, 69–82. https://doi.org/10.1016/j.jaerosci.2006.10.002.
Park, K., Kittelson, D.B., McMurry, P.H., 2004a. Structural properties of diesel exhaust particles measured by transmission electron microscopy (TEM): relationships to particle mass and mobility. Aerosol Sci. Technol. 38, 881–889. https://doi.org/10.1080/027868290505189.
Park, K., Kittelson, D.B., Zachariah, M.R., McMurry, P.H., 2004b. Measurement of inherent material density of nanoparticle agglomerates. J. Nanopart. Res. 6, 267–272. https://doi.org/10.1023/B:NANO.0000034657.71309.e6.
Pei, X.Y., Hallquist, M., Eriksson, A.C., Pagels, J., Donahue, N.M., Mentel, T., Svenningsson, B., Brune, W., Pathak, R.K., 2018. Morphological transformation of soot: investigation of microphysical processes during the condensation of sulfuric acid and limonene ozonolysis product vapors. Atmos. Chem. Phys. 18, 9845–9860. https://doi.org/10.5194/acp-18-9845-2018.
Peng, J.F., Hu, M., Guo, S., Du, Z.F., Zheng, J., Shang, D.J., Zamora, M.L., Zeng, L.M., Shao, M., Wu, Y.S., Zheng, J., Wang, Y., Glen, C.R., Collins, D.R., Molina, M.J., Zhang, R.Y., 2016. Markedly enhanced absorption and direct radiative forcing of black carbon under polluted urban environments. Proc. Natl. Acad. Sci. U. S. A. 113, 4266–4271.
Peng L., Bi X., 2020. Comment on "Retrieval of Atmospheric Fine Particulate Density Based on Merging Particle Size Distribution Measurements: Multi-instrument Observation and Quality Control at Shouxian" by Li et al. J. Geophys. Res.: Atmos. 125, e2019JD031806. doi:https://doi.org/10.1029/2019JD031806.
Pitz, M., Cyrys, J., Karg, E., Wiedensohler, A., Wichmann, H.E., Heinrich, J., 2003. Variability of apparent particle density of an urban aerosol. Environ. Sci. Technol. 37, 4336–4342. https://doi.org/10.1021/es034322p.
Pitz, M., Schmid, O., Heinrich, J., Birmili, W., Maguhn, J., Zimmermann, R., Wichmann, H.E., Peters, A., Cyrys, J., 2008. Seasonal and diurnal variation of $PM_{2.5}$ apparent particle density in urban air in Augsburg. Germany. Environ. Sci. Technol. 42, 5087–5093. https://doi.org/10.1021/es7028735.
Poschl, U., 2005. Atmospheric aerosols: composition, transformation, climate and health effects. Angew. Chem. Int. Edit. 44, 7520–7540. https://doi.org/10.1002/anie.200501122.
Poulain, L., Wu, Z., Petters, M.D., Wex, H., Hallbauer, E., Wehner, B., Massling, A., Kreidenweis, S.M., Stratmann, F., 2010. Towards closing the gap between hygroscopic growth and CCN activation for secondary organic aerosols - part 3: influence of the chemical composition on the hygroscopic properties and volatile fractions of aerosols. Atmos. Chem. Phys. 10, 3775–3785. https://doi.org/10.5194/acp-10-3775-2010.
Pratt, K.A., Prather, K.A., 2012. Mass spectrometry of atmospheric aerosol-recent developments and applications. Part II: on-line mass spectrometry techniques. Mass Spectrom. Rev. 31, 17–48. https://doi.org/10.1002/mas.20330.
Qiao, K., Wu, Z., Pei, X., Liu, Q., Shang, D., Zheng, J., Du, Z., Zhu, W., Wu, Y., Lou, S., Guo, S., Chan, C.K., Pathak, R.K., Hallquist, M., Hu, M., 2018. Size-resolved effective density of submicron particles during summertime in the rural atmosphere of Beijing. China. J. Environ. Sci. (China) 73, 69–77. https://doi.org/10.1016/j.jes.2018.01.012.
Quiros, D.C., Hu, S.H., Hu, S.S., Lee, E.S., Sardar, S., Wang, X.L., Olfert, J.S., Jung, H.J.S., Zhu, Y.F., Huai, T., 2015a. Particle effective density and mass during steady-state operation of GDI, PFI, and diesel passenger cars. J. Aerosol Sci. 83, 39–54. https://doi.org/10.1016/j.jaerosci.2014.12.004.
Quiros, D.C., Zhang, S., Sardar, S., Kamboures, M.A., Eiges, D., Zhang, M., Jung, H.S., McCarthy, M.J., Chang, M.C.O., Ayala, A., Zhu, Y., Huai, T., Hu, S., 2015b. Measuring particulate emissions of light duty passenger vehicles using integrated particle size distribution (IPSD). Environ. Sci. Technol. 49, 5618–5627. https://doi.org/10.1021/acs.est.5b00666.
Rissler, J., Messing, M.E., Malik, A.I., Nilsson, P.T., Nordin, E.Z., Bohgard, M., Sanati, M., Pagels, J.H., 2013. Effective density characterization of soot agglomerates from various sources and comparison to aggregation theory. Aerosol Sci. Technol. 47, 792–805. https://doi.org/10.1080/02786826.2013.791381.
Rissler, J., Nordin, E.Z., Eriksson, A.C., Nilsson, P.T., Frosch, M., Sporre, M.K., Wierzbicka, A., Svenningsson, B., Löndahl, J., Messing, M.E., Sjogren, S., Hemmingsen, J.G., Loft, S., Pagels, J.H., Swietlicki, E., 2014. Effective density and mixing state of aerosol particles in a near-traffic urban environment. Environ. Sci. Technol. 48, 6300–6308. https://doi.org/10.1021/es5000353.
Ristimaki, J., Keskinen, J., 2006. Mass measurement of non-spherical particles: TDMA-ELPI setup and performance tests. Aerosol Sci. Technol. 40, 997–1001.
Rostedt, A., Marjamaki, M., Keskinen, J., 2009. Modification of the ELPI to measure mean particle effective density in real-time. J. Aerosol Sci. 40, 823–831.
Saathoff, H., Naumann, K.H., Mohler, O., Jonsson, A.M., Hallquist, M., Kiendler-Scharr, A., Mentel, T.F., Tillmann, R., Schurath, U., 2009. Temperature dependence of yields of secondary organic aerosols from the ozonolysis of alpha-pinene and limonene. Atmos. Chem. Phys. 9, 1551–1577. https://doi.org/10.5194/acp-9-1551-2009.
Sarangi, B., Aggarwal, S.G., Sinha, D., Gupta, P.K., 2016. Aerosol effective density measurement using scanning mobility particle sizer and quartz crystal microbalance with the estimation of involved uncertainty. Atmos. Meas. Tech. 9, 859–875. https://doi.org/10.5194/amt-9-859-2016.
Schmid, O., Karg, E., Hagen, D.E., Whitefield, P.D., Ferron, G.A., 2007. On the effective density of non-spherical particles as derived from combined measurements of aerodynamic and mobility equivalent size. J. Aerosol Sci. 38, 431–443. https://doi.org/10.1016/j.jaerosci.2007.01.002.
Schneider, J., Weimer, S., Drewnick, F., Borrmann, S., Helas, G., Gwaze, P., Schmid, O., Andreae, M.O., Kirchner, U., 2006. Mass spectrometric analysis and aerodynamic properties of various types of combustion-related aerosol particles. Int. J. Mass Spectrom. 258, 37–49. https://doi.org/10.1016/j.ijms.2006.07.008.
Schnitzler, E.G., Dutt, A., Charbonneau, A.M., Olfert, J.S., Jaeger, W., 2014. Soot aggregate restructuring due to coatings of secondary organic aerosol derived from aromatic precursors. Environ. Sci. Technol. 48, 14309–14316. https://doi.org/10.1021/es503699b.
Seinfeld, J.H., Pandis, S.N., 2016. Atmospheric Chemistry and Physics: From Air Pollution to Climate Change: John Wiley & Sons.
Slowik, J.G., Stainken, K., Davidovits, P., Williams, L.R., Jayne, J.T., Kolb, C.E., Worsnop, D.R., Rudich, Y., DeCarlo, P.F., Jimenez, J.L., 2004. Particle morphology and density characterization by combined mobility and aerodynamic diameter measurements. Part 2: application to combustion-generated soot aerosols as a function of fuel equivalence ratio. Aerosol Sci. Technol. 38, 1206–1222. https://doi.org/10.1080/027868290903916.
Slowik, J.G., Cross, E.S., Han, J.H., Kolucki, J., Davidovits, P., Williams, L.R., Onasch, T.B., Jayne, J.T., Kolb, C.E., Worsnop, D.R., 2007. Measurements of morphology changes of fractal soot particles using coating and denuding experiments: implications for optical absorption and atmospheric lifetime. Aerosol Sci. Technol. 41, 734–750. https://doi.org/10.1080/02786820701432632.
Spencer, M.T., Prather, K.A., 2006. Using ATOFMS to determine OC/EC mass fractions in particles. Aerosol Sci. Technol. 40, 585–594. https://doi.org/10.1080/02786820600729138.
Spencer, M.T., Shields, L.G., Prather, K.A., 2007. Simultaneous measurement of the effective density and chemical composition of ambient aerosol particles. Environ. Sci. Technol. 41, 1303–1309. https://doi.org/10.1021/es061425+.

Stein, M., Kiesler, D., Kruis, F.E., 2013. Adjustment and online determination of primary particle size in transferred arc synthesis of copper nanoparticles. Aerosol Sci. Technol. 47, 1276–1284.

Su, Y.X., Sipin, M.F., Furutani, H., Prather, K.A., 2004. Development and characterization of an aerosol time-of-flight mass spectrometer with increased detection efficiency. Anal. Chem. 76, 712–719. https://doi.org/10.1021/ac034797z.

Sumlin, B.J., Oxford, C.R., Seo, B., Pattison, R.R., Williams, B.J., Chakrabarty, R.K., 2018. Density and homogeneous internal composition of primary brown carbon aerosol. Environ. Sci. Technol. 52, 3982–3989. https://doi.org/10.1021/acs.est.8b00093.

Tang I.N., Munkelwitz H.R., 1994. Water activities, densities, and refractive-indexes of aqueous sulfates and sodium-nitrate droplets of atmospheric importance. J. Geophys. Res.: Atmos. 99, 18801–18808.

Tavakoli, F., Olfert, J.S., 2014. Determination of particle mass, effective density, mass-mobility exponent, and dynamic shape factor using an aerodynamic aerosol classifier and a differential mobility analyzer in tandem. J. Aerosol Sci. 75, 35–42. https://doi.org/10.1016/j.jaerosci.2014.04.010.

Vaden, T.D., Imre, D., Beranek, J., Zelenyuk, A., 2011. Extending the capabilities of single particle mass spectrometry: II. Measurements of aerosol particle density without DMA. Aerosol Sci. Technol. 45, 125–135. https://doi.org/10.1080/02786826.2010.526156.

Varutbangkul, V., Brechtel, F.J., Bahreini, R., Ng, N.L., Keywood, M.D., Kroll, J.H., Flagan, R.C., Seinfeld, J.H., Lee, A., 2006. Hygroscopicity of secondary organic aerosols formed by oxidation of cycloalkenes, monoterpenes, sesquiterpenes, and related compounds. Atmos. Chem. Phys. 6, 2367–2388.

Virtanen, A., Ristimäki, J., Keskinen, J., 2004. Method for measuring effective density and fractal dimension of aerosol agglomerates. Aerosol Sci. Technol. 38, 437–446. https://doi.org/10.1080/02786820490445155.

Wu, Y.F., Xia, Y.J., Huang, R.J., Deng, Z.Z., Tian, P., Xia, X.G., Zhang, R.J., 2019. A study of the morphology and effective density of externally mixed black carbon aerosols in ambient air using a size-resolved single-particle soot photometer (SP2). Atmos. Meas. Tech. 12, 4347–4359.

Xie, Y.Y., Ye, X.N., Ma, Z., Tao, Y., Wang, R.Y., Zhang, C., Yang, X., Chen, J.M., Chen, H., 2017. Insight into winter haze formation mechanisms based on aerosol hygroscopicity and effective density measurements. Atmos. Chem. Phys. 17, 7277–7290. https://doi.org/10.5194/acp-17-7277-2017.

Yin, Z., Ye, X., Jiang, S., Tao, Y., Shi, Y., Yang, X., Chen, J.M., 2015. Size-resolved effective density of urban aerosols in Shanghai. Atmos. Environ. 100, 133–140. https://doi.org/10.1016/j.atmosenv.2014.10.055.

Yon, J., Bescond, A., Ouf, F.X., 2015. A simple semi-empirical model for effective density measurements of fractal aggregates. J. Aerosol Sci. 87, 28–37. https://doi.org/10.1016/j.jaerosci.2015.05.003.

Zelenyuk, A., Cai, Y., Chieffo, L., Imre, D., 2005. High precision density measurements of single particles: the density of metastable phases. Aerosol Sci. Technol. 39, 972–986. https://doi.org/10.1080/02786820500380206.

Zelenyuk, A., Cai, Y., Imre, D., 2006. From agglomerates of spheres to irregularly shaped particles: determination of dynamic shape factors from measurements of mobility and vacuum aerodynamic diameters. Aerosol Sci. Technol. 40, 197–217. https://doi.org/10.1080/02786820500529406.

Zelenyuk, A., Imre, D., Han, J.H., Oatis, S., 2008a. Simultaneous measurements of individual ambient particle size, composition, effective density, and hygroscopicity. Anal. Chem. 80, 1401–1407. https://doi.org/10.1021/Ac701723v.

Zelenyuk, A., Yang, J., Song, C., Zaveri, R.A., Imre, D., 2008b. "Depth-profiling" and quantitative characterization of the size, composition, shape, density, and morphology of fine particles with SPLAT, a single-particle mass spectrometer. J. Phys. Chem. A 112, 669–677.

Zelenyuk, A., Yang, J., Song, C., Zaveri, R.A., Imre, D., 2008c. A new real-time method for determining particles' sphericity and density: application to secondary organic aerosol formed by ozonolysis of alpha-pinene. Environ. Sci. Technol. 42, 8033–8038. https://doi.org/10.1021/es8013562.

Zelenyuk, A., Reitz, P., Stewart, M., Imre, D., Loeper, P., Adams, C., Andrie, M., Rothamer, D., Foster, D., Narayanaswamy, K., Najt, P., Solomon, A., 2014. Detailed characterization of particulates emitted by pre-commercial single-cylinder gasoline compression ignition engine. Combust. Flame 161, 2151–2164. https://doi.org/10.1016/j.combustflame.2014.01.011.

Zelenyuk, A., Wilson, J., Imre, D., Stewart, M., Muntean, G., Storey, J., Prikhodko, V., Lewis, S., Eibl, M., Parks, J., 2017. Detailed characterization of particulate matter emitted by lean-burn gasoline direct injection engine. Int. J. Engine Res. 18, 560–572.

Zhai, J.H., Lu, X.H., Li, L., Zhang, Q., Zhang, C., Chen, H., Yang, X., Chen, J.M., 2017. Size-resolved chemical composition, effective density, and optical properties of biomass burning particles. Atmos. Chem. Phys. 17, 7481–7493. https://doi.org/10.5194/acp-17-7481-2017.

Zhang, G.H., Bi, X.H., Han, B.X., Qiu, N., Dai, S.H., Wang, X.M., Sheng, G.Y., Fu, J.M., 2016a. Measurement of aerosol effective density by single particle mass spectrometry. Sci. China Earth Sci. 59, 320–327. https://doi.org/10.1007/s11430-015-5146-y.

Zhang, Y.X., Zhang, Q., Cheng, Y.F., Su, H., Kecorius, S., Wang, Z.B., Hu, M., Zhu, T., 2016b. Measuring the morphology and density of internally mixed black carbon with SP2 and VTDMA: new insight into the absorption enhancement of black carbon in the atmosphere. Atmos. Meas. Tech. 9, 1833–1843. https://doi.org/10.5194/amt-9-1833-2016.

Zhao, G., Tan, T.Y., Zhao, W.L., Guo, S., Tian, P., Zhao, C.S., 2019. A new parameterization scheme for the real part of the ambient urban aerosol refractive index. Atmos. Chem. Phys. 19, 12875–12885. https://doi.org/10.5194/acp-19-12875-2019.

Zhao, S.P., Yu, Y., Yin, D.Y., He, J.J., 2017. Effective density of submicron aerosol particles in a typical valley city, western China. Aerosol Air Qual. Res. 17, 1–13. https://doi.org/10.4209/aaqr.2015.11.0641.